



Numerical evaluation of cohesive and adhesive failure modes during the indentation of coated systems with compliant substrates



Newton K. Fukumasu^{*}, Roberto M. Souza

Surface Phenomena Laboratory, Polytechnic School of the University of Sao Paulo, Sao Paulo, Brazil

ARTICLE INFO

Available online 17 August 2014

Keywords:

FEM
Crack propagation
Indentation
Coating

ABSTRACT

The indentation of coated systems allows the analysis of the mechanical properties of each individual constituent, or of the entire system, including material constitutive behavior and failure properties. Due to the progressive loading and unloading of the indentation cycle, both cohesive and adhesive failures can occur in the coating and at the coating/substrate interface, respectively. In this work, the Finite Element Method (FEM) was applied to develop a numerical model based on a spherical rigid indenter in contact with a coated compliant substrate. The coating behavior was defined based on the properties of brittle pure elastic materials, while the substrate was assumed elastic-perfectly plastic. Both cohesive and adhesive failure models were included in the analyses, allowing the evaluation of failure in the coating and/or at the coating/substrate interface. The eXtended Finite Element Method (XFEM) was applied to reproduce the cohesive cracks through the coating thickness, while the Cohesive Zone Model (CZM) was used to evaluate the coating/substrate interfacial crack. System failure was analyzed considering a range of coating parameters (elastic modulus, fracture toughness, energy release rate for cohesive propagation, thickness and residual stresses), coating/substrate interface properties (interface toughness and adhesive crack energy release rate) and the radius of the spherical indenter. The range of input values resulted in simulations with cohesive and/or adhesive failures and allowed determination of a parameter that presented good correlation with the occurrence of crack propagation and failure. Cohesive failures in the coating also produced signatures on the load–displacement (P–h) indentation curves, which allowed the evaluation of coating fracture toughness with good agreement with the input toughness values in cases where the coating was thin.

© 2014 Elsevier B.V. All rights reserved.

1. Introduction

In the past decades, many works have been dedicated to the analysis of the indentation process in coated systems [1]. One of the key approaches in this type of study is the use of the Finite Element Method (FEM) to analyze how stress and strain distributions are affected by geometrical and material characteristics of both the coating and the substrate [2–8]. Literature also presents works using the FEM to study the failure of coated systems during the indentation process, by means of the interpretation of stress and strain distributions as the source of nucleation and propagation of cracks in the coating (cohesive) or along the coating/substrate interface (adhesive) [9–15]. Furthermore, in at least two works [15,16] geometrical and material characteristics of the system were organized in order to map either the location of initial cohesive cracking [15] or the position of yield inception in the

coated system [15,16]. More recently, Lu and Chou [17] validated discontinuous techniques to simulate the nucleation and propagation of cracks during indentation and the effect over stress and strain distributions.

Micro and nanoindentation analyses have also been included as part of the methods for mechanical characterization of coated systems. In those cases, information from indentation load–displacement curves has been used to calculate coating hardness and elastic modulus [22–25], as well as fracture toughness [26] and residual stresses [27–30].

In this work, 220 FEM simulations were conducted varying geometrical characteristics (coating thickness and spherical indenter radius), materials and interface properties (coating elastic modulus, fracture resistance of the coating and fracture resistance of the interface), as well as the level of coating residual stresses. In all cases, criteria were defined to analyze the nucleation and propagation of cohesive and adhesive cracks. The failure of the system during the indentation process resulted on unique features observed in load–displacement curves. Those features allowed the analysis of a literature method for calculation of coating fracture toughness. In addition, the combination

^{*} Corresponding author.

E-mail address: newton.fukumasu@gmail.com (N.K. Fukumasu).

of geometrical and material parameters, used as simulation inputs, allowed the development of a new parameter that presents good correlation with the occurrence of cohesive cracks during the indentation process.

2. Model description

In this work, 2D axisymmetric numerical models of an indentation cycle were developed using the Abaqus® finite element environment. The model was solved based on static ramped load, in which time derivatives and inertial loads were disregarded.

The indentation models were based on a spherical rigid indenter pushed against a coated compliant substrate. Fig. 1 shows a schematic representation of the indentation system, in which t is the coating thickness and R_i is the indenter radius. The substrate height and the system diameter were both constrained at 250.0 μm for all analyses. This system was discretized with approximately 63,000 continuum axisymmetric quadrilateral elements.

The coating was modeled considering fully-elastic mechanical behavior, determined by the coating elastic modulus (E_c) and the coating Poisson's ratio (ν_c). The substrate was defined as an elastic-perfectly plastic material, in which the mechanical behavior is determined by the substrate elastic modulus (E_s), the substrate Poisson's coefficient (ν_s) and the substrate yield stress (σ_s). The Von Mises criterion was selected to indicate the onset of substrate plastic deformation.

Two techniques were applied to include discontinuity effects on the stress and strain distributions due to the nucleation and propagation of both cohesive and adhesive cracks: the eXtended Finite Element Method (XFEM) and the cohesive zone model (CZM). Both the XFEM and CZM techniques are based on the traction-separation constitutive behavior, which models the failure of the system with a linear elastic behavior followed by the initiation and evolution of damage. Details on these techniques may be found elsewhere [17–20].

The XFEM enabled the analyses to consider cohesive failure, allowing the evaluation of both nucleation and propagation of cracks in the coating independently of mesh distribution or refinements. In this technique, a crack is nucleated based on a fracture initiation criterion, such as the maximum principal stress, maximum principal strain or maximum quadratic stresses, and propagates according to a damage evolution criterion based on energy release rate or opening length of the crack. Each crack generated by this technique, as implemented in the Abaqus environment, demands an exclusive XFEM region. In this

work, a total of 50 XFEM regions were created in the coating to allow multiple spatial cohesive crack nucleation and propagation. The length of each zone was set constant for all analyses at 2.0 μm , parallel to the radial direction, as shown in Fig. 1.

The coating/substrate interface, which represents a discontinuous variation of material properties, was modeled as a plain perfectly bonded surface with negligible thickness. The CZM was used to evaluate the damage and possible delamination of the interface, reproducing the adhesive failure of the coating. Similar to the XFEM, the CZM technique also requires a fracture initiation criterion and a damage evolution law.

For crack propagation, two models are implemented in Abaqus: propagation by energy dissipation and crack opening displacement. In this work, a linear damage evolution law based on the energy dissipation was selected for both failure techniques (XFEM and CZM) [18,21]. A small value of $2.0 \cdot 10^{-5}$ was used as damage stabilization to improve the solution convergence [17,18]. The fracture initiation criterion for adhesive failure of the coating/substrate interface, based on CZM, was defined as a maximum principal stress of $\sigma_{\text{CZM}} = 75$ MPa constant for all analyses. This value was selected to ensure good interface adhesion and is consistent with values available in the literature [18,19]. Variations in σ_{CZM} would imply interfaces with different quality in terms of adhesion, which was not analyzed in this work.

The fracture initiation criterion for cohesive cracks in the coating, based on XFEM, was selected as the maximum principal strain (ϵ_c), given by Eq. (1). In this equation, which is consistent with a pure elastic behavior, a_c is the critical crack length defined, in this work, as 5% of the minimum element characteristic length. The fracture toughness of the coating (K_c) is given by Eq. (2), in which G_c is the energy release rate for cohesive failure.

$$\epsilon_c = \frac{K_c(1-\nu^2)}{E_c} \frac{1}{\sqrt{\pi a_c}} \quad (1)$$

$$K_c = \sqrt{G_c E_c}. \quad (2)$$

Before the indentation procedure, a homogeneous residual stress (σ_c) was applied to the mesh elements of the coating. The boundaries of the system considered constrains on both radial and tangential directions at the axis of symmetry (Fig. 1) and on both radial and vertical directions at the bottom of the substrate. The indentation cycle consisted of two steps: normal loading with 1.0 N and the unloading of the indenter. In both steps, loads varied linearly over the integration time.

In all simulations, the elastic modulus (E_s), Poisson's ratio (ν_s) and Yield stress (σ_s) of the substrate, as well as Poisson's ratio of the coating (ν_c), were kept constant, with values of 69.0 GPa, 0.3, 180.0 MPa and 0.3, respectively. Table 1 shows ranges of variation of other input parameters, which were combined to provide a total of 220 numerical simulations.

The values of coating fracture toughness, evaluated by Eq. (2), were varied in the range between 3.4 and 14.4 $\text{MPa}\sqrt{\text{m}}$, which are compatible with literature values for stiff coatings [26,31,32].

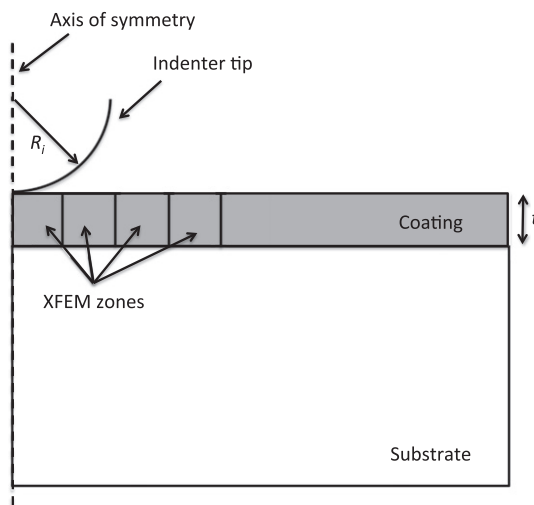


Fig. 1. Schematic representation of the indentation system based on a spherical indenter in contact to a coated compliant substrate. t is the coating thickness and R_i is the indenter radius.

Table 1

Range of values of input variables considered in the simulation of the spherical indentation of coated systems.

Variable	Range of values
Coating thickness (t)	0.25 or 4.0 μm
Indenter radius (R_i)	200.0 or 400.0 μm
Elastic modulus of the coating (E_c)	232.5 to 825.0 GPa
Energy release rate for cohesive failure (G_c)	0.05 to 0.25 mJ/mm^2
Energy release rate for adhesive failure (G_{int})	0.025 to 0.25 mJ/mm^2
Residual stress in the coating (σ_c)	– 10.0 to 3.0 GPa

3. Results and discussion

3.1. Signatures on the load–displacement curves

The indentation analyses in this work were such that, as a general trend, the nucleation and propagation of cohesive cracks in the coating occurred only during the loading portion of the indentation cycle, while adhesive failure of the coating/substrate interface occurred during the unloading portion of the test. Then, variations on the load–displacement curves can be associated with specific phenomena, such as cohesive failure during loading and adhesive failure during the unloading step.

Fig. 2 shows load–displacement curves, that are representative of the responses obtained with the combinations of input variables. Fig. 2a presents a regular curve with one pop-in [8,9,14,23,33] close to the end of the loading step, while Fig. 2b indicates multiple pop-ins during the indentation stage. Fig. 2c represents a curve of a simulation system with no cohesive failure during the loading portion of the indentation.

Fig. 3a and b indicates the distribution of maximum principal stresses in the coating before and after a pop-in on the load–displacement curve of a simulation that resulted in significant propagation of one single crack (as in Fig. 2a). Fig. 3c and d presents the stress distribution of a simulation with significant propagation of multiple cracks (as in Fig. 2b). Fig. 3e presents the distribution of maximum principal stresses of a simulation with no cohesive failure (as in Fig. 2c). The substrate is omitted for better visualization, since no adhesive failure was observed during the loading portion of the indentation cycle.

Figs. 2 and 3 confirmed that the pop-in events on the load–displacement curves are directly related to the propagation of cohesive cracks in the coating, allowing the evaluation of the coating fracture toughness [26]. Nevertheless, Fig. 3a and b indicates that cohesive cracks may not propagate through the entire coating thickness during a single pop-in, as assumed in the procedure for the evaluation of coating properties. Table 2 shows the values of coating toughness calculated based on the method proposed by Li and Bhushan [26], for a set of numerical analyses in which only the coating thickness was modified. This table indicates that the literature [26] method presents better results for systems with coating thickness below 250 nm. This result is probably explained by the fact that, in thicker coatings, pop-ins are associated with cohesive cracks that do not propagate along the entire coating thickness.

Fig. 3c and d shows multiple crack propagations in the coating. Part of the cracks was nucleated at the coating surface and others at the coating/substrate interface. In order to explain the stress distributions, one may note that bending tensile stresses develop at the coating/substrate interface in the regions close to the axis of symmetry of the model. These tensile stresses may be increased by coating stretching at the same region, resulting in the nucleation and propagation of cracks from the interface toward the surface of the coating [13,14]. Bending tensile stresses also develop at the coating surface in the region close to the indentation edge, promoting crack nucleation at the surface [10,11].

The parameters selected in all the simulations of this work resulted in some degree of adhesive failure at the coating/substrate interface during the unloading step, as a result of the entirely elastic behavior defined for the coating. In a pure elastic material, all strain energy is stored as elastic deformations that tend to restore the original shape once the loading is removed. Thus, with the elevated degree of plastic deformation in the substrate, the elastic coating induces high axial stresses at coating/substrate interface, leading to mode I failure. Although all simulations presented some degree of adhesive failure, no significant variations on the load–displacement curves were observed during the unload portion of the indentation cycle.

3.2. Threshold for cohesive failure of a coating

Parameter F_1 was defined (Eq. (3)) to analyze the combined effect of input variables analyzed in this work. This parameter presents a direct

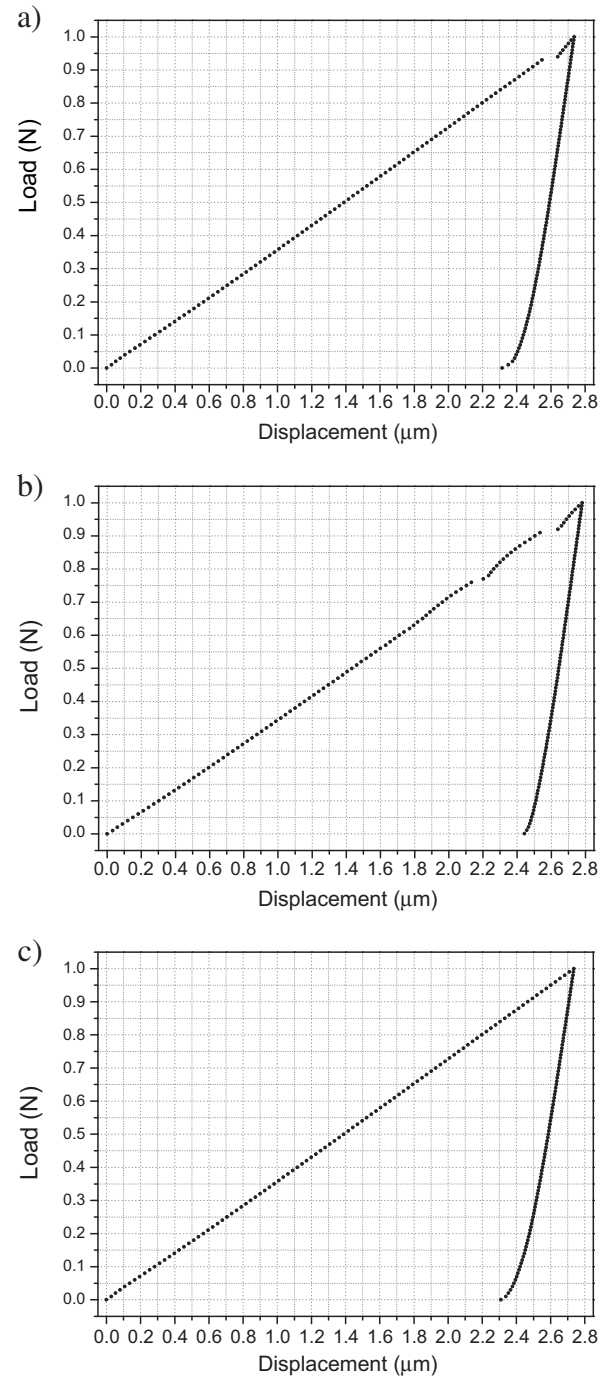


Fig. 2. Signatures on the load–displacement curves of the failure on the coating during the indentation process: a) single cohesive failure on the coating; b) multiple cohesive failures on the coating and c) no cohesive failure on the coating.

relationship with the applied load P , the radius of the indenter R_i and the fracture toughness of the coating K_c , as well as an inverse relationship with the elastic modulus of the coating E_c and the coating thickness t . In addition, parameter F_1 presents an inverse relationship with the area of contact (A), calculated directly from the finite element software, considering the length of elements of the coating that are in contact with the rigid indenter at maximum load.

$$F_1 = \frac{P R_i^2 K_c^3}{A \sqrt{t E_c}} \quad (3)$$

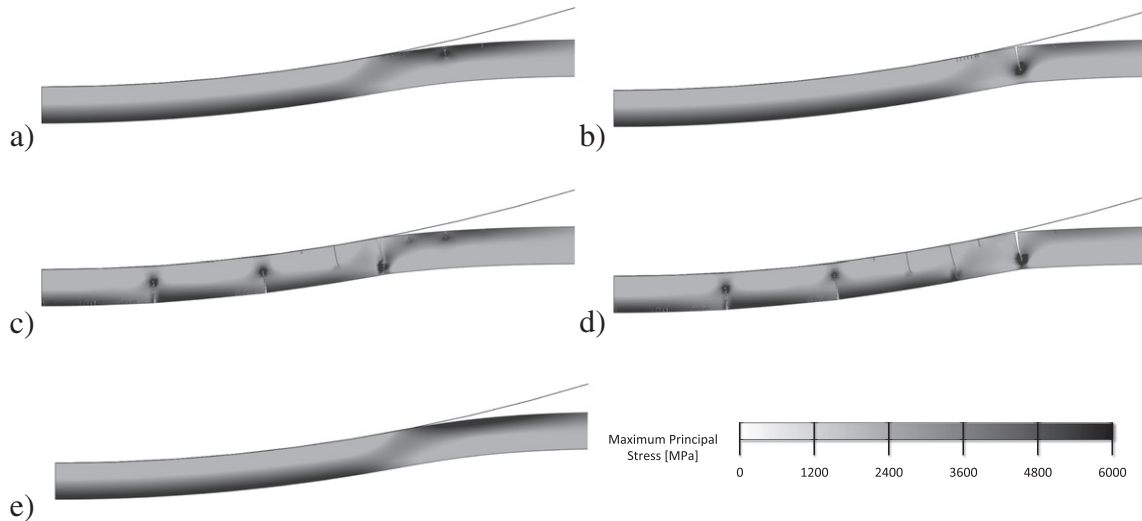


Fig. 3. Distribution of principal stress of the coating during the loading portion of the indentation cycle: a) single crack before the pop-up of Fig. 2a; b) single crack after the pop-up of Fig. 2a; c) multiple cracks before the last pop-up of Fig. 2b; d) multiple cracks after the last pop-up of Fig. 2b and e) image of no cohesive failure. Both the substrate is omitted and the scale was clipped in the range of 0 to 6000 MPa to allow better visualization. No adhesive failure was seen during the loading step.

Fig. 4 presents the values of F_1 obtained for all the simulations of this work, plotted as a function of coating toughness K_c . In this figure, a horizontal dark gray line was drawn to separate the great majority of the simulations presenting cohesive failure (filled symbols) from those where only adhesive failure was observed (empty symbols). The few points that do not follow the general trend will be discussed below. If these points are not considered, and for the ranges covered in this work, F_1 approximately equal to 2.0 represents a threshold of significant technological interest, above which there was no observation of significant cohesive crack propagation.

In order to associate physical meaning to parameter F_1 , it is convenient to observe that, at first, the area of contact A could not be considered a direct input parameter. However, if this value is analyzed in conjunction with the applied load, as P/A , it may be recognized as an indication of the system resistance to deformation, i.e. hardness. Thus, larger P/A values are associated with shallower penetration depths.

Along these lines, for a given penetration depth, the radius R_i of the indenter will be also responsible for the amount of deformation, i.e. for the amount of bending and stretching observed in different regions of the coating [10]. In this case, deformation would present an inverse relationship with R_i . Then, if $(PR_i^2)/A$ presents an inverse correlation with strain, $(PR_i^2)/(AE_c)$ would have an inverse correlation with stress. In Fig. 5, $(PR_i^2)/(AE_c)$ is plotted as a function of radial stresses in the coating, which are the stresses responsible for the nucleation and propagation of cohesive cracks in the coating (Fig. 3). Fig. 5a presents the maximum radial stresses at the coating/substrate interface and close to the axis of symmetry of the model, for a group of simulations in which only the coating thickness was varied and the highest value of K_c was selected, avoiding the influence of discontinuities (cohesive failures) on stress distributions. Fig. 5b presents similar results for the coating surface and at the region close to the indentation edge. Overall,

Fig. 5 indicates that a significant portion of parameter F_1 , $(PR_i^2)/(AE_c)$, presents good correlation with the stresses responsible for cohesive cracking, reflecting the increase in surface radial stresses at the indentation edge as $(PR_i^2)/(AE_c)$ decreases. Fig. 5 also presents effects of coating thickness, indicating that thicker coatings would be prone for cohesive cracking from surface to interface at the model edge and thinner coatings would be prone for cohesive cracking from interface to the surface in regions close to the axis of symmetry. These differences may reflect the need for inclusion of coating thickness in the calculation of F_1 .

The effect of coating thickness may also be considered when one observes that, in coated systems, the P/A value becomes more related to the mechanical properties of the substrate as the applied load increases or the coating thickness decreases [25]. Fig. 6 presents the variation of P/A as a function of coating thickness for a group of simulations in which only the value of coating thickness was varied. This figure shows an increase of P/A for thicknesses higher than $0.5 \mu\text{m}$, indicating that, above this value, it is not precise to neglect the contribution of coating properties to the behavior of the systems analyzed in this work. In Fig. 4, cases presenting both cohesive cracks and F_1 higher than 2.0 represent analyses with coating thickness equal or lower than $0.5 \mu\text{m}$.

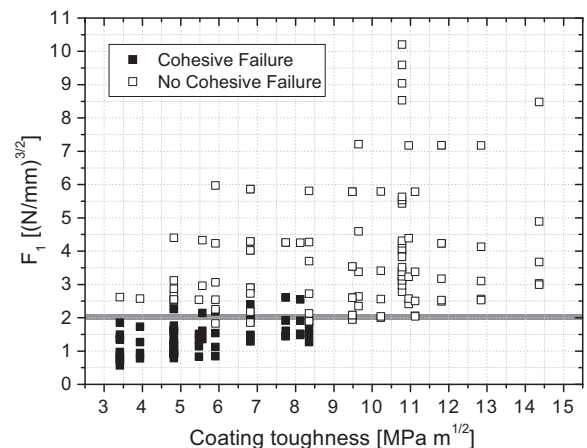


Fig. 4. Values of parameter F_1 as a function of coating toughness. The dark gray line represents the threshold between the occurrences of cohesive failure (filled symbols) and only adhesive failure (empty symbols).

Table 2

Application of Li's method [26] to calculate coating fracture toughness. Results for a set of simulations with the same input variables, except for coating thickness. The input value for coating fracture toughness was $4.83 \text{ MPa}\sqrt{\text{m}}$.

Coating thickness [μm]	Calculated coating toughness [$\text{MPa}\sqrt{\text{m}}$]	Variation with respect to input value [%]
0.12	4.79	0.62
0.25	4.42	8.30
0.50	0.97	79.87
1.00	0.74	84.64

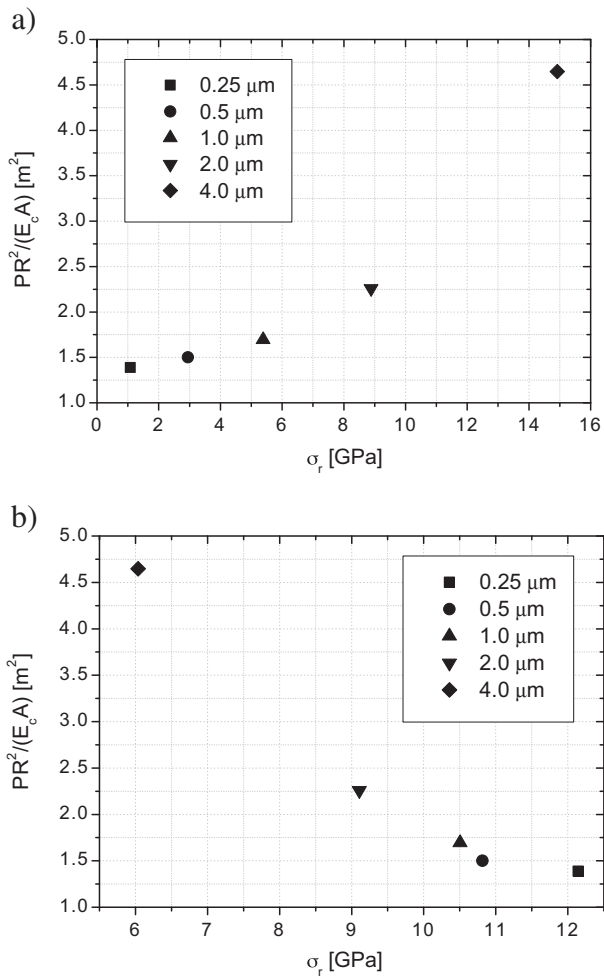


Fig. 5. Values of $(PR^2)/(AE_c)$ as a function of coating maximum radial stresses (σ_r) at a region: a) close the axis of symmetry of the model and b) close to the indentation edge. This figure presents a group of simulations in which only the coating thickness (symbols) was varied and the coating toughness was selected as the highest value to avoid the influence of discontinuities (cohesive failures) on stress distributions.

As shown in Fig. 4, in such conditions there is a less substantial contribution of the coating properties to the P/A value. These cases do not follow the trend presented in Fig. 4, since there is not a significant increase in P/A as t decreases. Then, higher values of F_1 are calculated without the reduction of the bending stresses, leading to the trend of more coating cracking

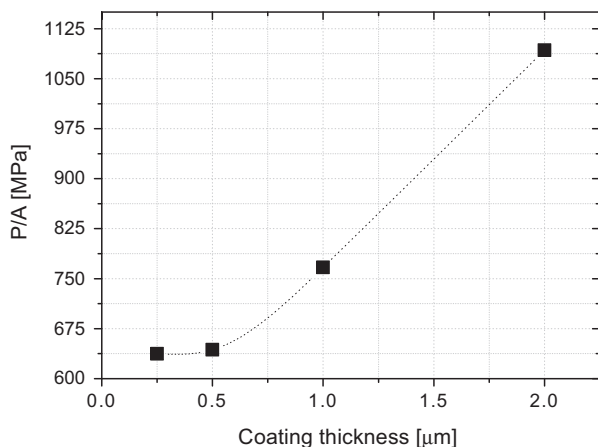


Fig. 6. Values of P/A obtained from the simulations for four different coating thicknesses.

as the thickness decreases, as observed experimentally [9,10]. Thus, the trend represented by the horizontal line in Fig. 4 may be considered valid as long as the coating presents a thickness large enough to significantly affect the system deformation under the applied load. In those cases, the expected decrease in F_1 (higher tendency for cohesive cracking) with the increase of t (Eq. (3)), is compensated by an increase in F_1 due to the increase of P/A , as shown in Fig. 6.

Finally, some comments may be addressed regarding the effect of coating residual stresses. In Fig. 4, a horizontal line separates most of the conditions with or without cohesive cracking. Therefore, it is not possible to associate and increase, or decrease, in the critical value of F_1 with the change in K_c . Since the threshold line is horizontal, the same trend would be observed independently of the variable selected as the x-axis. This result was not expected initially, particularly in terms of the value of the coating residual stress, which was not included in the calculation of parameter F_1 and has already been reported as an important variable regarding coating fracture [34]. One attempt to analyze the effect of coating residual stresses is their effect in P/A . As previously published [29,30,35], residual stresses may be responsible for a change in the area of contact. For example, an increase in the area of contact is observed with the presence of compressive residual stresses. However, those cases are also associated with an increase in the load needed to reach a given penetration depth, such that the value of P/A could remain similar.

In order to explore this point with further detail, Fig. 7 presents the variation of F_1 as a function of coating residual stress for two groups of simulations in which both the coating toughness and the residual stress were changed. The first group considered an elevated coating toughness ($K_c = 10.8 \text{ MPa } \sqrt{\text{m}}$), for which no cohesive failure is expected. For this group, white squares in Fig. 7 indicate a decrease in F_1 with the decrease in residual stress. However, F_1 presents an asymptotic behavior in which the threshold would not be reached even for extreme, and unrealistic, compressive residual stresses. In other words, for this particular case, despite the decrease in F_1 with the increase in compressive residual stress values, F_1 will remain above the limit, indicating the absence of cohesive fracture, as expected for an increase in compressive residual stresses. The second group was selected with a lower coating toughness ($K_c = 4.8 \text{ MPa } \sqrt{\text{m}}$), represented in Fig. 7 by filled square symbols. This group indicates a reduced influence of residual stresses on F_1 for brittle coatings, due to the relief of coating stresses on regions close to a crack that has propagated.

4. Conclusions

In this work, 2D axisymmetric FEM analyses of one indentation cycle were carried out to identify unique signatures on the load–displacement

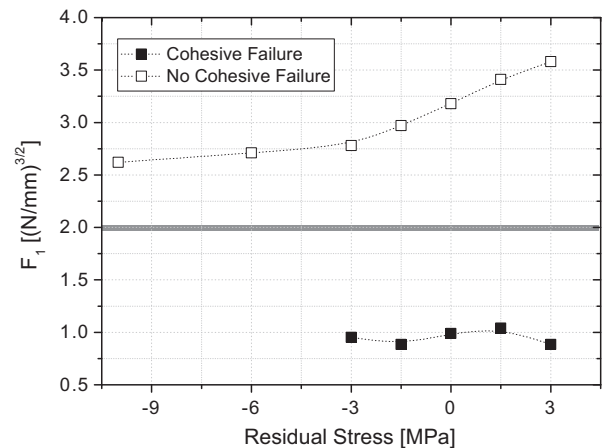


Fig. 7. Values of P/A as a function of coating residual stress. Negative residual stresses indicate a compressive stress on the coating in directions parallel to the coating surface.

curves, produced by the failure of the coating and coating/substrate interface. The simulations conducted with the selected range of the input parameters showed that:

- the coupled XFEM and CZM techniques allowed the realistic reproduction of failure behavior of coated systems under indentation loads, such as the cohesive failure produced exclusively during the loading of the system and the adhesive failure of the interface predominantly during the unloading portion of the cycle;
- the realistic simulation of the failures also allowed the correlation between unique signatures on the load–displacement curve and cohesive crack propagation, allowing the use of these signatures to calculate the fracture toughness of the coating for cracks that propagate through the entire thickness of the coating;
- from the analyses of the bending and stretching of the coating, a parameter F_1 was established as a threshold for the occurrence of cohesive cracks in the coating. The threshold value observed for the simulations in this work was valid as long as the contribution of the coating is significant in the overall deformation of the system.
- the coating residual stress was considered in the calculation of parameter F_1 through P/A , however, for the analyzed parameters range, the variation on residual stresses presented an asymptotic behavior toward the F_1 threshold.

Acknowledgments

The authors recognize the National Council for Scientific and Technological Development-CNPq for the financial support through processes 380172/2010-0 and 303780/2008-8.

References

- [1] J. Mackerle, *Eng. Comput.* 21 (2004) 23.
- [2] K. Komvopoulos, *Trans. ASME: J. Tribol.* 111 (1989) 430.
- [3] H. Djabella, R.D. Arnell, *Thin Solid Films* 213 (1992) 205.
- [4] P. Montmitonet, M.L. Edlinger, E. Felder, *Trans. ASME: J. Tribol.* 115 (1993) 477.
- [5] M.R. Begley, A.G. Evans, J.W. Hutchinson, *Int. J. Solids Struct.* 36 (1999) 2773.
- [6] N.K. Fukumasu, R.M. Souza, *Surf. Coat. Technol.* 201 (2006) 4294.
- [7] L.G.D.B.S. Lima, L.C.S. Nunes, R.M. Souza, N.K. Fukumasu, A. Ferrarese, *Surf. Coat. Technol.* 215 (2013) 327.
- [8] S. Kataria, S. Goyal, S. Dash, R. Sandhya, M.D. Mathew, A.K. Tyagi, *Thin Solid Films* 522 (2012) 297.
- [9] E. Weppelmann, M.V. Swain, *Thin Solid Films* 286 (1996) 111.
- [10] R.M. Souza, A. Sinatora, G.G.W. Mustoe, J.J. Moore, *Wear* 250–251 (2001) 1337.
- [11] R.M. Souza, G.G.W. Mustoe, J.J. Moore, *Thin Solid Films* 392 (2001) 65.
- [12] T. Pachler, R.M. Souza, A.P. Tschiptschin, *Surf. Coat. Technol.* 202 (2007) 1098.
- [13] A. Abdul-Baqi, E. Van der Giessen, *Int. J. Solids Struct.* 39 (2002) 1427.
- [14] M.T. Tilbrook, D.J. Paton, Z. Xie, M. Hoffman, *Acta Mater.* 55 (2007) 2489.
- [15] M. Kot, W. Rakowski, J.M. Lackner, L. Major, *Mater. Des.* 43 (2013) 99.
- [16] W. Song, L. Li, I. Etsion, A. Ovcharenko, F.E. Talke, *Surf. Coat. Technol.* 240 (2014) 444.
- [17] P. Lu, K. Chou, *Proc. ASME Int. Manuf. Sci. Eng. Conf.* 2013.
- [18] H. Rehman, F. Ahmed, C. Schmid, J. Schaufler, K. Durst, *Surf. Coat. Technol.* 207 (2012) 163.
- [19] J.Y. Faou, G. Parry, S. Grachev, E. Barthel, *Phys. Rev. Lett.* 108 (2012) 116102.
- [20] N. Chandra, H. Li, C. Shet, H. Ghonem, *Int. J. Solids Struct.* 39 (2002) 2827.
- [21] L. Chen, K.B. Yeap, C.M. She, G.R. Liu, *Eng. Struct.* 33 (2011) 3269.
- [22] W.D. Nix, *Mater. Sci. Eng. A Struct. Mater.* 234–236 (1997) 37.
- [23] B. Bhushan, X. Li, *Int. Mater. Rev.* 48 (2003) 125.
- [24] T.F. Page, S.V. Hainsworth, *Surf. Coat. Technol.* 61 (1993) 201.
- [25] S.A.R. Pulecio, M.C.M. Farias, R.M. Souza, *Surf. Coat. Technol.* 205 (2010) 1386.
- [26] X. Li, B. Bhushan, *Thin Solid Films* 315 (1998) 214.
- [27] J. Jang, *J. Ceram. Process. Res.* 10 (2009) 391.
- [28] E. Atar, C. Sarioglu, U. Demirler, E. Sabri Kayali, H. Cimenoglu, *Scripta Mater.* 48 (2003) 1331.
- [29] C.E.K. Mady, S.A. Rodriguez, A.G. Gomez, R.M. Souza, *Surf. Coat. Technol.* 205 (2010) 1393.
- [30] C.E.K. Mady, S.A. Rodriguez, A.G. Gomez, R.M. Souza, *J. Mater. Res.* 27 (2012) 1732.
- [31] X. Li, D. Diao, B. Bhushan, *Acta Mater.* 45 (1997) 4453.
- [32] G.K. Beshish, C.W. Florey, F.J. Worzala, W.J. Lenling, *J. Thermal Spray Technol.* 2 (1993) 35.
- [33] Z.-H. Xie, M. Hoffman, R.J. Moon, P.R. Munroe, *J. Mater. Res.* 21 (2006) 437.
- [34] S. Bhowmick, V. Jayaram, S.K. Biswas, *Acta Mater.* 53 (2005) 2459.
- [35] A. Bolshakov, W.C. Oliver, G.M. Pharr, *J. Mater. Res.* 11 (1996) 760.